Monthly Notices
of the
ROYAL ASTRONOMICAL SOCIETY

MNRAS **505,** 2009–2019 (2021)
Advance Access publication 2021 May 19

https://doi.org/10.1093/mnras/stab1414

Peculiarities of the chemical abundance distribution in galaxies NGC 3963 and NGC 7292

A. S. Gusev ★ and A. V. Dodin

Sternberg Astronomical Institute, Lomonosov Moscow State University, Universitetsky pr. 13, 119234 Moscow, Russia

Accepted 2021 May 11. in original form 2021 April 27

ABSTRACT

Spectroscopic observations of 32 H II regions in the spiral galaxy NGC 3963 and the barred irregular galaxy NGC 7292 were carried out with the 2.5-m telescope of the Caucasus Mountain Observatory of the Sternberg Astronomical Institute using the Transient Double-beam Spectrograph with a dispersion of ≈1 Å pixel^{-1} and a spectral resolution of ≈3 Å. These observations were used to estimate the oxygen and nitrogen abundances and the electron temperatures in H II regions through modern strong-line methods. In general, the galaxies have oxygen and nitrogen abundances typical of stellar systems with similar luminosities, sizes, and morphology. However, we have found some peculiarities in chemical abundance distributions in both galaxies. The distorted outer segment of the southern arm of NGC 3963 shows an excess oxygen and nitrogen abundances. Chemical elements abundances in NGC 7292 are constant and do not depend on the galactocentric distance. These peculiarities can be explained in terms of external gas accretion in the case of NGC 3963 and major merging for NGC 7292.

Key words: ISM: abundances – H II regions – galaxies: abundances – galaxies: individual: NGC 3963, NGC 7292.

1 INTRODUCTION

The distribution of chemical elements in galaxies plays a key role in understanding their formation and evolution. Regions of ionized hydrogen with their bright emission spectra are good indicators of this distribution. The oxygen abundance is usually used as a tracer of current metallicity in spiral and irregular galaxies. Numerous spectroscopic observations of H II regions, beginning from Searle (1971), reveal an exponential decrease in the oxygen-to-hydrogen ratio from the centre to the outer disc regions of galaxies.

Chemical elements gradients are the result of the galaxy evolution, where a complex interplay between star formation rate and efficiency, stellar migration, accretion and outflow of metal-poor and metal-rich gas, tidal interactions and mergers, as well as gas flows within the disc form the radial distribution of heavy chemical elements (Zurita et al. 2021a). The findings of investigations into variations of the gas composition within galaxies, in combination with results on the evolution of stellar populations, have led to the development of models of chemical evolution of galaxies (Chiappini et al. 2003; Marcon-Uchida et al. 2010).

Studies of possible relationships between the abundance properties and global characteristics of galaxies such as morphology and luminosity are equally important (Pagel 1991; Vila-Costas & Edmunds 1992; Dutil & Roy 1999; Sánchez et al. 2014; Florido et al. 2015; Pérez-Montero et al. 2016; Zinchenko et al. 2019; Zurita et al. 2021b).

Although the main indicator of metallicity is the oxygen abundance, the nitrogen-to-oxygen ratio plays an equally important role, being an indicator of star formation history (Mallery et al. 2007; Mollá & Gavilán 2010).

To determine parameters of the oxygen and nitrogen abundance distributions, the abundance estimates for H II regions, evenly distributed across the whole galaxy disc from the inner to the outer part, are necessary. This kind of measurements are available for a few hundred galaxies (see compilations in Pilyugin et al. 2014; Zurita et al. 2021a).

Integral field unit spectroscopy instruments and large surveys associated with them provide the most complete data for chemical and kinematic analysis. However, a small field of view of such devices (74 × 64 arcsec^2 in CALIFA, for instance) confines the study of giant and nearby galaxies to their inner parts. Wide-field integral spectroscopy instruments provide observational data for smaller number of galaxies. We believe that classical long-slit and multislit spectroscopic data still play an important role, especially for studies of some individual galaxies with signs of peculiarity in morphology, which were not included in large spectral surveys.

The newly installed Transient Double-beam Spectrograph (TDS; see Section 2.1 for details) is already used actively in several large international projects such as the SRG/eROSITA All-Sky Survey (Dodin et al. 2020) and the Zwicky Transient Facility survey (Malanchev et al. 2021), as well as in various stellar, galactic, and extragalactic studies (see Potanin et al. 2020, and references therein). This paper presents the first results of a spectroscopic study of extragalactic H II regions obtained at the TDS.

We selected for spectroscopic study the Milky Way-type galaxy NGC 3963 and the Large Magellanic Cloud-type galaxy NGC 7292 (Fig. 1, Table 1). Both galaxies host numerous H II regions. NGC 3963 is a rather symmetric grand-design galaxy with distorted outer part of southern spiral arm. It has a companion of comparable mass, NGC 3958, which is located at the distance of 7.7 arcmin (110 kpc) to the south from NGC 3963. Tidal distortions have been found in both galaxies of the pair (van Moorsel 1983).

★ E-mail: gusev@sai.msu.ru

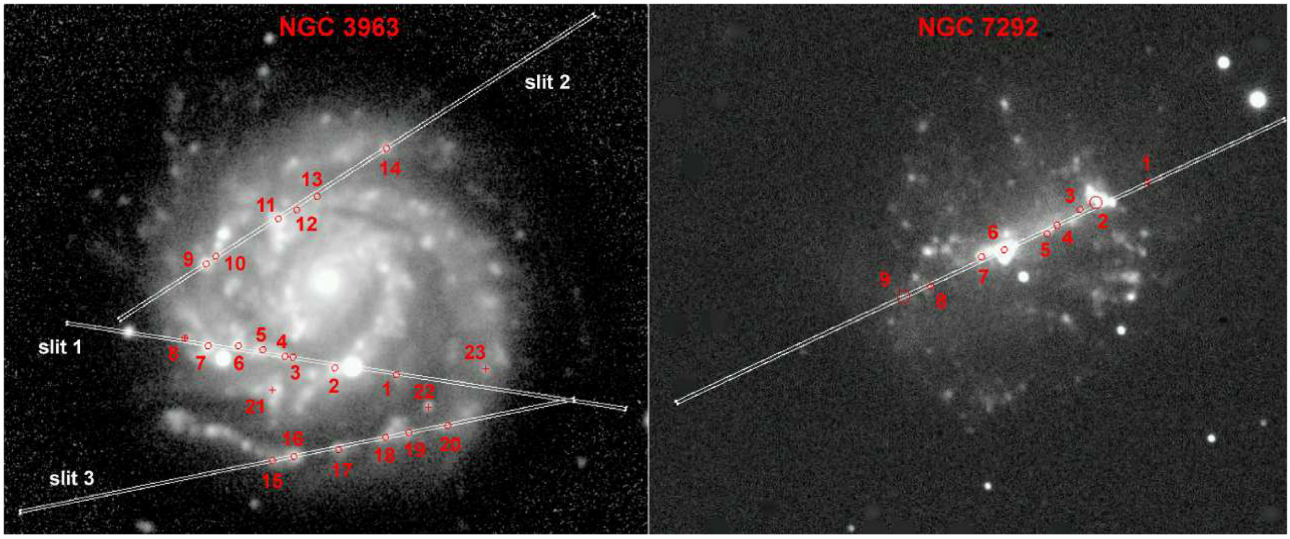

Figure 1. *U* images of NGC 3963 (left) and NGC 7292 (right) with overlaid positions of the slits (white narrow bars). The size of slits used is 180 × 1 arcsec^2. The positions and numbers of the H II regions observed via TDS (open red circles) and obtained from the SDSS (red crosses) are indicated. The region no. 8 in NGC 3963 (cross in circle) was observed both with the TDS and BOSS (SDSS). North is upwards and east is to the left.

Table 1. The galaxy sample.

Galaxy	Type	B_t (mag)	M_B^a (mag)	Inclination (deg)	PA (deg)	v^b (km s^{-1})	R_{25}^c (arcmin)	R_{25}^c (kpc)	d (Mpc)	$A(B)_{\rm Gal}$ (mag)	$A(B)_{\rm in}$ (mag)
1	2	3	4	5	6	7	8	9	10	11	12
NGC 3963	SAB(rs)bc	12.60 ± 0.07	−21.10 ± 0.325	28.9	95.9	3184	1.285	18.39	49.2	0.083	0.09
NGC 7292	IBm	13.06 ± 0.06	−17.00 ± 1.007	54.4	113.0	986	0.953	1.89	6.82	0.223	0.32

Notes. [a] Absolute magnitude of a galaxy corrected for Galactic extinction and inclination effects.
[b]Heliocentric radial velocity.
[c]Radius of a galaxy at the isophotal level 25 mag arcsec^{-2} in the *B* band corrected for Galactic extinction and inclination effects.

NGC 7292 is an irregular galaxy with a strong bright bar. The galaxy looks like a flower with three petals with the bar between two of them (Fig. 1). Let us remark that Magellanic-type galaxies is a rare galactic type. Data on the chemical elements abundance in H II regions in this type of stellar systems are known for a limited number of galaxies (see e.g. Pilyugin et al. 2014, and references therein).

Both galaxies are not isolated and are influenced by the environment: gas accretion in the case of NGC 3963 and a major merging in the case of NGC 7292. The goal of our study is to check how the environment affects the chemical elements abundance and their spatial distribution in these galaxies.

Spectroscopic observations of H II regions in NGC 3963 and NGC 7292 have not been carried out previously, with the exception of four regions, which were observed in the Sloan Digital Sky Survey[1] (SDSS). These regions are included in our study (see Fig. 1).

The fundamental parameters of the galaxies are presented in Table 1, where the morphological type, Galactic absorption, $A(B)_{\rm Gal}$, and the distance to NGC 3963 are taken from the NED[2] data base, and the remaining parameters are taken from the LEDA[3] data base. The distance to NGC 7292 is still an open question (see the distance estimates in NED). We use the value of the distance to NGC 7292 obtained in Tully et al. (2009).

[1]https://www.sdss.org
[2]http://ned.ipac.caltech.edu
[3]http://leda.univ-lyon1.fr

2 OBSERVATIONS AND DATA REDUCTION

2.1 Observations

The observations were carried out at the 2.5 m telescope of the Caucasus Mountain Observatory of the Sternberg Astronomical Institute (Lomonosov Moscow State University; CMO SAI MSU) with the TDS. This is a new device which was installed at the end of 2019 (Potanin et al. 2020).

The spectrograph operates simultaneously in blue (the range of 3600–5770 Å with a dispersion of 1.21 Å pixel^{-1} and a spectral resolution of 3.6 Å) and red (the range of 5673–7460 Å with a dispersion of 0.87 Å pixel^{-1} and a spectral resolution of 2.6 Å) channels (Potanin et al. 2020). Two CCD cameras use E2V 42-10 detectors with a size of 2048 × 512 pixels^2. The pixel size is 0.363 arcsec, the size of slits used is 180 × 1 arcsec^2. For a detailed description of the spectrograph, see Potanin et al. (2020).

Observations were carried out in 2020 December (see the journal of observations in Table 2). An example of raw spectrum obtained in both channels is presented in Fig. 2 (top panel).

We chose such slit positions to cover the maximum number of H II regions in a wide range of galactocentric distances. As a result, we obtained spectra for 20 H II regions in NGC 3963 and nine H II regions in NGC 7292 (Fig. 1).

Spectral data for objects in NGC 3963 were obtained using three slit positions (H II region nos. 1–8 were covered by the first, nos. 9–14 by the second, and nos. 15–20 by the third slit position; see Fig. 1).

Table 2. Journal of observations.

Slit position	PA_{slit} (deg)	Date	Exposures (s)	Air mass
		NGC 3963		
1	81.2	2020.12.11/12	900 × 4	1.1
2	123.0	2020.12.14/15	900 × 3	1.6
3	101.7	2020.12.17/18	900 × 6	1.5
		NGC 7292		
	118.3	2020.12.10/11	100 + 900 × 3	1.4

Four H II regions in NGC 3963 have been previously observed in the SDSS with the BOSS spectrograph (nos. 8, 21–23). The region no. 8 in NGC 3963 was observed both on the TDS and BOSS (Fig. 1). One-dimensional spectra of these objects[4] were downloaded from the SDSS DR 16 data base.[5]

The seeing during our observations was from 1.2 up to 1.8 arcsec, typical angular diameters of studied H II regions are from 2 up to 7 arcsec (Fig. 1). Remark that the last observational night was cloudy, as a result the spectra obtained in the slit position 3 have a lower signal-to-noise ratio.

The observing procedure involved obtaining flat and wavelength calibration images at the beginning and end of each set. Spectrophotometric standards were observed immediately after the studied objects at the same airmass.

2.2 Data reduction

Initial data reduction followed routine procedures, including dark, cosmic ray, and flat-field corrections, wavelength calibration with a standard Ne-Al-Si lamp, rebinning the data on to a uniform wavelength grid, wavelength correction using night sky lines, photometric calibration, summation of spectra, subtracting the background, and transformation to one-dimensional spectrum (see Potanin et al. 2020, for details). To reduce raw spectra, we used a PYTHON-based data processing package, developed in SAI MSU, and the European Southern Observatory Munich Image Data Analysis System (ESO-MIDAS). An example of final 2D spectrum is presented in Fig. 2 (bottom panel). An example of 1D spectrum after reduction is shown in Fig. 3.

The emission-line fluxes were measured using the continuum-subtracted spectrum. Flux calibration was performed, using standard stars BD+75°325, HZ21, and HR4554 from the ESO list.[6]

The extraction aperture corresponded to the area, where the brightest emission lines from H II regions were 'visible' above the noise. This size is approximately equal to the angular diameter of individual H II regions projected along the PA of the slit. Thus the apparent sizes of the studied H II regions are larger than the width of the slit.

Coordinates, deprojected galactocentric distances of H II regions, the logarithmic extinction coefficient $c(\mathrm{H}\beta)$, equivalent widths of the H α and H β lines, and undereddened H β line fluxes are listed in Table 3. We also give in this table the electron densities, n_e, of H II regions obtained from the [S II]λ6717/[S II]λ6731 ratio according to Proxauf et al. (2014).

[4]Files: spec-8234-57450-0784.fits (no 8), spec-8237-58162-0466.fits (no 21), spec-8234-57450-0786.fits (no 22), and spec-8237-58162-0462.fits (no. 23)
[5]http://skyserver.sdss.org/dr16
[6]https://www.eso.org/sci/observing/tools/standards.html

When calculating the error of the line flux measurement, we took into account the following factors: the Poisson statistics of the line photon flux, the error connected with the computation of the underlying continuum, and the uncertainty of the spectral sensitivity curve. All these components are summed in quadrature. The total errors have been propagated to calculate the errors of all derived parameters. The use of the 1 arcsec slit introduces an unknown factor up to 2 due to slit losses, which, however, is constant within 3 percent over the spectral range.

The measured emission fluxes F were corrected for the interstellar reddening and Balmer absorption in the underlying stellar continuum. The theoretical H α/H β ratio from Osterbrock (1989), assuming case B recombination and an electron temperature of 10^4 K and the analytical approximation to the Whitford interstellar reddening law by Izotov et al. (1994), were used. We adopted the absorption equivalent width of hydrogen lines $\mathrm{EW}_a(\lambda) = 2$ Å according to McCall et al. (1985), and $\mathrm{EW}_a(\lambda) = 0$ for lines other than hydrogen.

Reddening-corrected line intensities $I(\lambda)/I(\mathrm{H}\beta)$ are given in Table 4.

3 RESULTS

3.1 Preliminary remarks

As we noted above, the H II region no. 8 in NGC 3963 was observed with both TDS and BOSS. We compared our measurements from the TDS spectrum with results from the BOSS spectrum in Fig. 4. As seen from the figure, the fluxes, obtained from the TDS and BOSS spectra, coincide within the error limits for all main emission lines.

At the same time, the fluxes obtained in the BOSS spectrum turned out to be 1.9 ± 0.2 times higher than in the TDS spectrum. This is obviously due to the different apertures used. The BOSS has a 3 arcsec round aperture, while on the TDS a 1 arcsec width slit is used.

The measurement errors for emission lines, obtained from the BOSS spectrum, turned out to be significantly smaller than those obtained from the TDS spectrum. This is due to the fact that object no. 8 is one of two faintest objects in our sample, so it has relatively large errors in measured fluxes and $c(\mathrm{H}\beta)$ (see Table 4). An additional factor is that the SDSS spectra have already been corrected for reddening, so we do not take into account their $c(\mathrm{H}\beta)$ errors. Further, we will use the results of measurements of the region no. 8 in NGC 3963, obtained from the BOSS spectrum.

As is known, emission spectra can be created by different excitation mechanisms. We examined the studied H II regions on the emission-line diagnostic diagram [N II]λ6584/H α versus [O III]λ5007/H β (Baldwin et al. 1981).

Fig. 5 shows that most of H II regions from our sample are definitely thermally photoionized objects, that is, classical H II regions. Three regions of our sample (no. 16 in NGC 3963 and nos. 1 and 4 in NGC 7292) are located near the border separating objects with thermal and non-thermal emissions. These objects will be discussed in Section 4.3. Nevertheless, all these H II regions are included in further consideration.

It should be noted that the samples of H II regions in galaxies NGC 3963 and NGC 7292 are located on the diagram in Fig. 5 separately from each other. Objects in NGC 3963 have a systematically lower [O III]λ5007/H β ratio and a higher [N II]λ6584/H α ratio than those in NGC 7292.

We eliminated from further consideration H II regions with large errors in the measured line fluxes. Basically, these errors are the

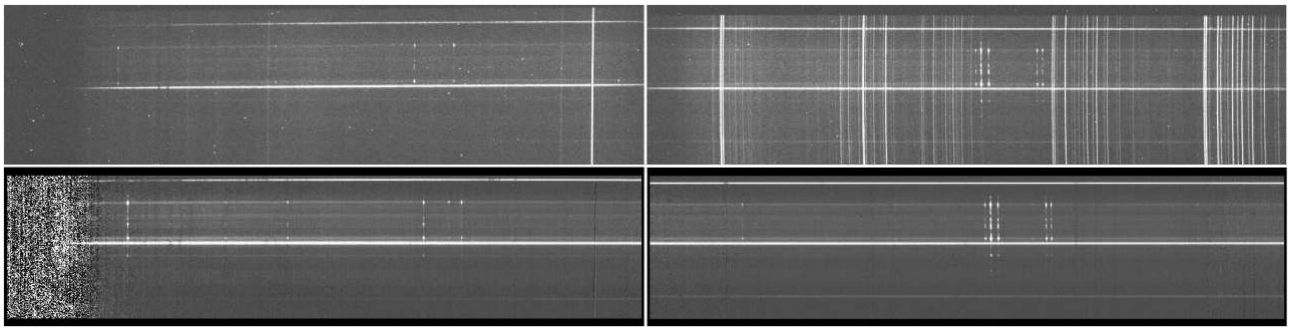

Figure 2. Frames with spectra of NGC 3963 obtained in the position of slit 1 in blue (left-hand panels) and red (right-hand panels) channels of the TDS. The raw spectra (top) and the spectra after initial reduction (bottom) are shown. The sizes of the images are 2048 × 512 (top) and 2030 × 460 pixels^2 (bottom).

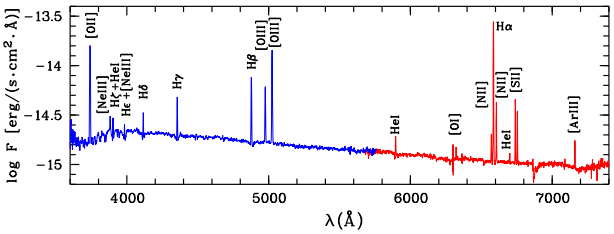

Figure 3. The spectrum of the HII region no. 6 (nucleus) of NGC 7292. The spectra obtained in the blue and red channels of the TDS are overlaid on one another.

result of large uncertainties in estimates of the extinction coefficient $c(\mathrm{H}\,\beta)$. The flux measurement errors are comparable to the fluxes themselves for all the main emission lines in region nos. 13, 15, and 16 in NGC 3963, in which $\Delta c(\mathrm{H}\,\beta) > 0.9$ (Table 3). These H II regions are not included in Table 4.

Extinction coefficients in H II region nos. 11 and 12 in NGC 3963 were estimated with errors of >0.5 (Table 3). As a result, the line fluxes were measured with an accuracy of ≈ 50 per cent (Table 4). Moreover, we were unable to measure [O III]λ4959 and [O III]λ5007 lines for these objects. These two regions were also excluded from further analysis.

3.2 Oxygen and nitrogen abundances

We are unable to use the direct T_e-method to estimate the oxygen and nitrogen abundances, since auroral lines in spectra of H II regions from our sample, such as [O III]λ4363 or [N II]λ5755, are too faint to be detected. Thus, we need to use empirical calibrations. Such methods are well developed (Kobulnicky & Kewley 2004; Pettini & Pagel 2004; Pilyugin & Thuan 2005; Bresolin 2007; Pilyugin et al. 2010; Pilyugin & Mattsson 2011; Marino et al. 2013; Pilyugin & Grebel 2016).

The most modern two-dimensional R and S-calibrations (Pilyugin & Grebel 2016) are the simplest and the most popular now. The R-calibration, based on the [O II] and [N II] strong emission lines, is more resistant to the presence of diffuse ionized gas (see e.g. Sanders et al. 2017; Kumari et al. 2019; Poetrodjojo et al. 2019), but it is sensitive to extinction errors. The S-method, based on the [N II] and [S II] lines, does not depend strongly on extinction, but it cannot be used for the nitrogen abundance estimates (Pilyugin & Grebel 2016). Among the other methods we distinguish the NS-calibration (Pilyugin & Mattsson 2011), which is based on the [O III], [N II], and [S II] emission-line intensities (see discussion in Gusev et al. 2012, 2014).

All the empirical calibrations are constructed under some assumptions. One of them is that the H II regions are in the low-density regime (Pilyugin & Mattsson 2011; Pilyugin & Grebel 2016), which is typical for the majority of extragalactic H II regions (Zaritsky et al. 1994; Bresolin et al. 2005; Gutiérrez & Beckman 2010).

The dependence n_e versus [S II]λ6717/[S II]λ6731 degenerates at low n_e (Proxauf et al. 2014), thus we give upper limits of n_e in Table 3 for most H II regions. Large upper limits of n_e for H II region nos. 12, 15, and 16 in NGC 3963 are rather a result of large line flux errors. However, one H II region of our sample, no. 6 in NGC 3963, is an apparently high-density object (see Table 3). The empirical calibrations are not applicable to such regions. As a result, this region was eliminated from further consideration.

We calculated the oxygen and nitrogen abundances in H II regions using three different calibrations discussed above. Data of emission lines fluxes from Table 4 were used. For several regions, where the [O III]λ4959 or [N II]λ6548 lines fluxes have not been measured, we adopt $I([\mathrm{O\,III}]\lambda4959+[\mathrm{O\,III}]\lambda5007) = 1.33I([\mathrm{O\,III}]\lambda5007)$ and $I([\mathrm{N\,II}]\lambda6548+[\mathrm{N\,II}]\lambda6584) = 1.33I([\mathrm{N\,II}]\lambda6584)$ according to results of Storey & Zeippen (2000).

The resultant oxygen abundances from the R, NS, and S-calibrations abundances, and nitrogen abundances from the R and NS-calibrations, and NS-calibration electron temperatures are given in Table 5.

Chemical elements abundance estimates obtained using various calibrations give small systematic shifts, ∼0.1 dex for oxygen and ∼0.15 dex for nitrogen. These are typical shifts between different empirical calibrations (see e.g. Kewley & Ellison 2008; Zurita et al. 2021a, and references therein). Remark that the intrinsic accuracy of strong lines methods is equal to 0.05–0.1 dex (Pilyugin et al. 2010; Pilyugin & Mattsson 2011; Pilyugin & Grebel 2016). These errors are not included in errors in Table 5.

Obtained oxygen and nitrogen abundances and electron temperatures are typical of galaxies with similar luminosities (see e.g. Zurita et al. 2021b). The O/H–N/O diagram (Fig. 6) illustrates this well. All our points lie within the spread of sample of best-studied H II regions in nearby galaxies, where the chemical elements abundances were derived using the direct T_e-method. The diagram shows that NGC 3963 is a system that is rich in oxygen and nitrogen, in which secondary nitrogen dominates. The nitrogen abundance in H II regions of NGC 3963 increases at a faster rate than the oxygen abundance. H II regions in NGC 7292 have lower oxygen abundance and a domination of primary nitrogen (Fig. 6).

Table 3. Parameters of H II regions, equivalent widths of the H α and H β lines, and undereddened H β line fluxes.

H II region	N–S[a] (arcsec)	E–W[a] (arcsec)	r^b (kpc)	r/R_{25}^b	c(H β)	n_e (cm^{-3})	EW(H α) (Å)	EW(H β) (Å)	F(H β) (10^{-16} erg s^{-1} cm^{-2})
					NGC 3963				
1	–30.0	+22.4	9.89	0.538	1.04 ± 0.15	<260	94.2 ± 17.1	18.7 ± 3.9	2.3 ± 0.2
2	–27.8	+2.9	7.60	0.413	0.99 ± 0.02	<130	185.1 ± 12.7	31.2 ± 2.4	29.6 ± 0.4
3	–24.6	–10.6	7.08	0.385	1.17 ± 0.08	<120	105.2 ± 10.4	21.5 ± 2.7	3.8 ± 0.2
4	–24.2	–13.1	7.20	0.392	0.87 ± 0.03	<130	155.6 ± 13.9	32.2 ± 4.3	9.1 ± 0.2
5	–22.0	–20.1	7.57	0.411	0.95 ± 0.08	<130	70.2 ± 7.6	16.0 ± 1.5	5.0 ± 0.3
6	–20.8	–28.0	8.63	0.469	1.30 ± 0.27	530 ± 220	62.0 ± 8.5	14.2 ± 1.9	1.7 ± 0.2
7	–20.8	–37.5	10.46	0.569	0.92 ± 0.02	<60	225.5 ± 18.1	33.1 ± 2.9	25.2 ± 0.3
8[c]	–18.2	–44.8	11.67	0.635	0.83 ± 0.30	<110	114.1 ± 69.2	20.9 ± 12.2	0.9 ± 0.2
8[d]	–18.2	–44.8	11.67	0.635	–	<110	60.9 ± 22.7	17.2 ± 2.5	1.8 ± 0.1
9	+5.6	–38.1	9.28	0.504	1.12 ± 0.05	<35	328.6 ± 112.6	42.3 ± 8.7	9.6 ± 0.2
10	+8.1	–35.0	8.70	0.473	0.88 ± 0.08	360 ± 190	217.5 ± 99.8	49.0 ± 22.4	4.6 ± 0.2
11	+20.1	–15.1	6.64	0.361	2.05 ± 0.55	<200	46.8 ± 5.4	9.8 ± 1.1	1.4 ± 0.3
12	+23.1	–9.2	6.71	0.365	1.59 ± 0.52	<580	61.9 ± 15.0	17.1 ± 4.1	1.2 ± 0.3
13	+27.2	–2.8	7.46	0.406	1.90 ± 0.92	<360	63.5 ± 17.7	15.7 ± 5.5	0.8 ± 0.3
14	+43.0	+19.4	12.46	0.678	1.05 ± 0.12	<120	214.1 ± 104.6	35.5 ± 16.0	4.6 ± 0.3
15	–57.7	–17.0	16.10	0.876	1.74 ± 1.37	<660	60.6 ± 23.1	13.3 ± 5.1	3.0 ± 1.6
16	–56.3	–10.2	15.44	0.840	2.01 ± 1.84	<870	46.5 ± 9.9	12.2 ± 2.9	2.9 ± 1.9
17	–54.0	+4.1	14.76	0.803	1.04 ± 0.10	<180	187.9 ± 64.2	32.3 ± 9.7	32.8 ± 1.8
18	–50.2	+18.9	14.51	0.789	0.92 ± 0.09	<130	125.7 ± 26.6	25.3 ± 5.3	28.6 ± 1.6
19	–48.7	+26.4	14.82	0.806	0.85 ± 0.14	<360	90.8 ± 23.3	21.7 ± 5.5	13.8 ± 1.4
20	–46.5	+38.9	15.89	0.864	1.20 ± 0.19	<250	67.6 ± 8.9	18.6 ± 3.5	16.3 ± 1.6
21	–35.0	–16.9	10.24	0.557	–	<110	34.4 ± 3.5	14.8 ± 1.7	1.5 ± 0.2
22	–40.4	+32.5	13.64	0.742	–	<85	194.4 ± 28.9	55.0 ± 9.3	11.0 ± 0.1
23	– 28.2	+51.0	14.56	0.792	–	<100	39.4 ± 5.7	13.5 ± 2.2	1.5 ± 0.1
					NGC 7292				
1	+18.5	+38.6	1.42	0.750	0.84 ± 0.20	<120	59.3 ± 12.1	19.9 ± 5.7	2.9 ± 0.4
2	+12.9	+24.7	0.93	0.490	0.68 ± 0.01	<40	152.9 ± 6.0	28.0 ± 1.2	108.7 ± 0.9
3	+11.0	+20.3	0.77	0.407	0.78 ± 0.02	<65	98.9 ± 5.8	23.6 ± 1.4	31.9 ± 0.6
4	+6.7	+14.3	0.52	0.277	1.12 ± 0.11	<40	48.9 ± 2.9	15.5 ± 1.0	9.2 ± 0.6
5	+4.5	+11.5	0.41	0.217	0.63 ± 0.05	<45	41.3 ± 2.0	14.7 ± 0.9	10.9 ± 0.6
6	0.0	0.0	0.00	0.000	0.57 ± 0.01	<60	117.3 ± 3.5	26.0 ± 0.9	226.4 ± 2.0
7	–1.8	–6.1	0.21	0.113	1.03 ± 0.04	<20	131.8 ± 7.5	25.1 ± 2.3	42.9 ± 0.9
8	–9.7	–19.5	0.72	0.382	0.98 ± 0.11	<30	79.1 ± 10.3	17.8 ± 2.6	9.2 ± 0.7
9	–12.8	–26.9	0.99	0.522	0.62 ± 0.06	<20	80.9 ± 13.6	22.0 ± 3.4	12.6 ± 0.7

Notes. [a] Offsets from the galactic centre, positive to the north and west.
[b]Deprojected galactocentric distance.
[c]From TDS spectrum.
[d]From SDSS spectrum.

3.3 Radial abundance gradients

Radial distributions of oxygen and nitrogen abundances, as well as electron temperatures, obtained using three different calibrations, are presented in Fig. 7.

Both galaxies show a peculiar radial abundance distribution. Both O/H and N/H decrease with distance from the galactic centre to distances of $r \approx 0.7R_{25}$ (13 kpc) in NGC 3963 (Fig. 7), which is common for spiral galaxies (Pilyugin et al. 2014). However, we find a flat distribution of oxygen and nitrogen abundances beyond these distances, at $r = 0.7 - 0.9R_{25}$. The flattening of radial oxygen abundance gradients in the outer parts of the discs in some giant galaxies was observed earlier. Ferguson et al. (1998) found it in NGC 628 at galactocentic distances $r > R_{25}$. Other similar examples are M83 and NGC 4625 (Pilyugin et al. 2012). However, this is a sufficiently rare occurrence. Among a sample of 130 nearby late-type galaxies from Pilyugin et al. (2014), we found only three galaxies with the steep inner ($r < 0.7 - 0.8R_{25}$) and flat outer distribution: NGC 1365, NGC 3621, and NGC 5457. All of them have signs of asymmetry in structure.

In the case of NGC 7292, we did not find any significant changes in oxygen and nitrogen abundances with distance from the centre (Fig. 7). Only one, the most distant H II region in this galaxy, is distinguished for its lower O/H and N/H abundances.

These peculiarities in chemical abundance distributions in both galaxies will be discussed in Section 4 in more detail.

To estimate radial oxygen and nitrogen abundances gradients, we used standard equations:

$$12 + \log(\mathrm{O/H}) = 12 + \log(\mathrm{O/H})_0 + C_{\mathrm{O/H}} r$$

and

$$12 + \log(\mathrm{N/H}) = 12 + \log(\mathrm{N/H})_0 + C_{\mathrm{N/H}} r,$$

where $12 + \log(\mathrm{O/H})_0$ and $12 + \log(\mathrm{N/H})_0$ are the extrapolated central oxygen and nitrogen abundances, $C_{\mathrm{O/H}}$ and $C_{\mathrm{N/H}}$ are the slopes of the oxygen and nitrogen abundances gradients, and r is the galactocentric distance.

The numerical values of the coefficients in the equations have been derived through the least squares method.

Table 4. The reddening-corrected fluxes of main emission lines of H II regions in units of $I(\mathrm{H}\,\beta)$.

H II region	[O II] 3727+3729	[O III] 4959	[O III] 5007	[N II] 6548	[N II] 6584	[S II] 6717	[S II] 6731
				NGC 3963			
1	5.88 ± 1.10	0.17 ± 0.09	0.50 ± 0.10	0.24 ± 0.05	0.78 ± 0.13	0.40 ± 0.07	0.30 ± 0.06
2	2.21 ± 0.10	0.06 ± 0.01	0.23 ± 0.01	0.30 ± 0.01	0.95 ± 0.02	0.36 ± 0.01	0.27 ± 0.01
3	4.02 ± 0.39	0.11 ± 0.04	0.33 ± 0.05	0.34 ± 0.03	1.06 ± 0.09	0.42 ± 0.04	0.30 ± 0.03
4	2.49 ± 0.13	0.10 ± 0.02	0.23 ± 0.02	0.33 ± 0.01	1.03 ± 0.04	0.39 ± 0.02	0.29 ± 0.01
5	3.36 ± 0.42	–	0.17 ± 0.05	0.32 ± 0.03	0.99 ± 0.09	0.49 ± 0.05	0.35 ± 0.04
6	8.44 ± 2.43	–	0.52 ± 0.13	0.28 ± 0.09	0.88 ± 0.25	0.49 ± 0.15	0.51 ± 0.15
7	3.53 ± 0.10	0.28 ± 0.02	0.78 ± 0.02	0.23 ± 0.01	0.75 ± 0.02	0.42 ± 0.01	0.29 ± 0.01
8	7.23 ± 0.55	0.13 ± 0.04	0.78 ± 0.08	0.28 ± 0.03	0.82 ± 0.06	0.67 ± 0.05	0.46 ± 0.04
9	3.03 ± 0.15	0.09 ± 0.02	0.45 ± 0.02	0.32 ± 0.02	0.84 ± 0.04	0.52 ± 0.03	0.34 ± 0.02
10	2.96 ± 0.25	0.12 ± 0.04	0.35 ± 0.05	0.32 ± 0.04	0.89 ± 0.08	0.36 ± 0.04	0.33 ± 0.04
11	14.71 ± 7.55	–	–	–	0.95 ± 0.52	0.49 ± 0.28	0.34 ± 0.20
12	5.49 ± 2.74	–	–	0.34 ± 0.18	1.07 ± 0.54	0.49 ± 0.26	0.41 ± 0.22
14	4.50 ± 0.56	0.24 ± 0.06	0.73 ± 0.08	0.30 ± 0.04	0.81 ± 0.10	0.51 ± 0.07	0.34 ± 0.05
17	4.49 ± 0.50	0.34 ± 0.06	0.70 ± 0.06	0.25 ± 0.03	0.78 ± 0.08	0.56 ± 0.07	0.41 ± 0.05
18	5.02 ± 0.49	0.37 ± 0.06	0.80 ± 0.07	0.30 ± 0.03	0.80 ± 0.08	0.61 ± 0.06	0.42 ± 0.05
19	5.01 ± 0.85	0.39 ± 0.10	0.55 ± 0.11	0.35 ± 0.07	0.93 ± 0.15	0.73 ± 0.13	0.60 ± 0.11
20	6.68 ± 1.39	0.36 ± 0.12	0.85 ± 0.14	0.32 ± 0.07	0.80 ± 0.15	0.52 ± 0.11	0.38 ± 0.08
21	7.75 ± 1.18	–	0.29 ± 0.09	0.30 ± 0.05	0.96 ± 0.11	0.68 ± 0.09	0.44 ± 0.07
22	2.40 ± 0.07	0.26 ± 0.01	0.74 ± 0.01	0.20 ± 0.01	0.60 ± 0.01	0.32 ± 0.01	0.23 ± 0.01
23	6.85 ± 0.79	0.31 ± 0.08	0.83 ± 0.10	0.31 ± 0.08	0.94 ± 0.09	0.84 ± 0.08	0.57 ± 0.06
				NGC 7292			
1	10.63 ± 2.43	1.37 ± 0.26	4.53 ± 0.69	–	0.38 ± 0.10	0.72 ± 0.17	0.46 ± 0.12
2	5.09 ± 0.07	0.86 ± 0.01	2.55 ± 0.02	0.09 ± 0.00	0.29 ± 0.00	0.42 ± 0.01	0.29 ± 0.00
3	5.41 ± 0.16	0.74 ± 0.02	2.07 ± 0.04	0.11 ± 0.01	0.42 ± 0.01	0.55 ± 0.02	0.39 ± 0.01
4	12.46 ± 1.43	0.85 ± 0.07	2.25 ± 0.16	0.18 ± 0.03	0.54 ± 0.07	0.82 ± 0.10	0.55 ± 0.07
5	8.65 ± 0.63	0.47 ± 0.05	1.47 ± 0.09	0.12 ± 0.02	0.52 ± 0.04	0.75 ± 0.06	0.50 ± 0.04
6	4.14 ± 0.05	0.70 ± 0.01	2.08 ± 0.02	0.10 ± 0.00	0.32 ± 0.00	0.32 ± 0.00	0.23 ± 0.00
7	5.80 ± 0.23	0.64 ± 0.02	2.03 ± 0.05	0.12 ± 0.01	0.36 ± 0.01	0.50 ± 0.02	0.32 ± 0.01
8	6.92 ± 0.86	0.46 ± 0.06	1.50 ± 0.12	0.17 ± 0.03	0.44 ± 0.06	0.67 ± 0.09	0.42 ± 0.06
9	5.74 ± 0.48	0.71 ± 0.06	1.75 ± 0.11	0.14 ± 0.03	0.42 ± 0.04	0.52 ± 0.04	0.31 ± 0.03

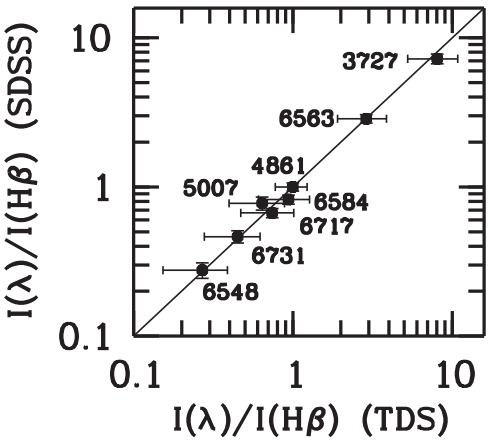

Figure 4. Comparison between reddening-corrected fluxes for the region no 8 in NGC 3963 obtained from the TDS and SDSS spectra. Corresponding wavelengths of spectral lines in Å are given. The error crosses are shown.

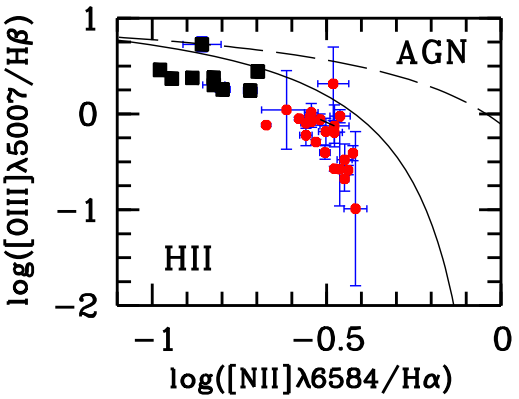

Figure 5. Emission-line diagnostic diagram for H II regions in NGC 3963 (small red circles) and NGC 7292 (large black squares). The curves separate objects with photoionized spectra from the objects with non-thermal emission spectra (AGN) according to Kauffmann et al. (2003) (solid curve) and Kewley et al. (2001) (dashed curve). The error crosses are shown.

For oxygen and nitrogen abundances in NGC 7292 as well as in the outer disc of NGC 3963 ($r \geq 0.7R_{25}$) we give the mean values.

Parameters of radial distributions of oxygen and nitrogen abundances in NGC 3963 and NGC 7292 are presented in Table 6.

Additionally, we calculated the central nitrogen-to-oxygen ratios, $\log(\mathrm{N/O})_0$, and the slopes of N/O gradient, $C_{\mathrm{N/O}}$, using the equation

$$\log(\mathrm{N/O}) = \log(\mathrm{N/O})_0 + C_{\mathrm{N/O}} r.$$

Fig. 7 and Table 6 show that the radial O/H and N/H gradients, obtained using different calibrations, coincide within slope errors. Both oxygen and nitrogen gradients in the inner part of NGC 3963 are typical for giant spiral galaxies (see e.g. Pilyugin et al. 2014; Zurita et al. 2021b).

Electron temperatures of H II regions anticorrelate with O/H and N/H abundances (Fig. 7). This anticorrelation, indicating that the

Table 5. Oxygen and nitrogen abundances and electron temperatures in H II regions derived using the R, NS, and S calibrations.

H II region	r/R_{25}	12+log(O/H)			12+log(N/H)		T_e
Calibration		R	NS	S	R	NS	NS
				NGC 3963			
1	0.538	8.44 ± 0.02	8.53 ± 0.01	8.49 ± 0.02	7.28 ± 0.05	7.62 ± 0.03	0.77 ± 0.02
2	0.413	8.57 ± 0.00	8.61 ± 0.00	8.56 ± 0.00	7.73 ± 0.01	7.89 ± 0.00	0.69 ± 0.01
3	0.385	8.56 ± 0.01	8.56 ± 0.01	8.58 ± 0.01	7.60 ± 0.02	7.83 ± 0.02	0.73 ± 0.02
4	0.392	8.58 ± 0.00	8.59 ± 0.00	8.58 ± 0.00	7.74 ± 0.01	7.88 ± 0.01	0.70 ± 0.01
5	0.411	8.55 ± 0.01	8.60 ± 0.01	8.54 ± 0.01	7.62 ± 0.03	7.84 ± 0.02	0.69 ± 0.03
7	0.569	8.47 ± 0.00	8.49 ± 0.00	8.48 ± 0.00	7.44 ± 0.01	7.52 ± 0.00	0.82 ± 0.00
8	0.635	8.45 ± 0.01	8.44 ± 0.00	8.46 ± 0.01	7.26 ± 0.02	7.42 ± 0.01	0.84 ± 0.01
9	0.504	8.53 ± 0.00	8.52 ± 0.00	8.51 ± 0.01	7.59 ± 0.01	7.64 ± 0.01	0.77 ± 0.01
10	0.473	8.54 ± 0.01	8.56 ± 0.01	8.54 ± 0.01	7.62 ± 0.02	7.76 ± 0.02	0.74 ± 0.01
14	0.678	8.49 ± 0.01	8.47 ± 0.01	8.49 ± 0.02	7.43 ± 0.03	7.53 ± 0.02	0.82 ± 0.01
17	0.803	8.47 ± 0.01	8.45 ± 0.01	8.46 ± 0.01	7.39 ± 0.03	7.44 ± 0.02	0.84 ± 0.01
18	0.789	8.47 ± 0.01	8.43 ± 0.01	8.47 ± 0.01	7.38 ± 0.02	7.42 ± 0.02	0.86 ± 0.01
19	0.806	8.52 ± 0.02	8.42 ± 0.01	8.49 ± 0.02	7.48 ± 0.04	7.42 ± 0.03	0.86 ± 0.01
20	0.864	8.46 ± 0.02	8.44 ± 0.01	8.49 ± 0.02	7.30 ± 0.05	7.47 ± 0.03	0.85 ± 0.01
21	0.557	8.49 ± 0.01	8.52 ± 0.01	8.50 ± 0.02	7.33 ± 0.04	7.63 ± 0.03	0.76 ± 0.03
22	0.742	8.46 ± 0.00	8.53 ± 0.00	8.45 ± 0.00	7.48 ± 0.01	7.55 ± 0.00	0.79 ± 0.00
23	0.792	8.50 ± 0.01	8.39 ± 0.01	8.48 ± 0.02	7.37 ± 0.03	7.36 ± 0.02	0.89 ± 0.01
				NGC 7292			
1	0.750	8.11 ± 0.04	8.30 ± 0.02	8.22 ± 0.04	6.58 ± 0.08	6.82 ± 0.05	1.07 ± 0.01
2	0.490	8.15 ± 0.00	8.26 ± 0.00	8.21 ± 0.00	6.75 ± 0.00	6.84 ± 0.00	1.00 ± 0.00
3	0.407	8.24 ± 0.00	8.31 ± 0.00	8.26 ± 0.00	6.91 ± 0.01	6.91 ± 0.01	0.97 ± 0.00
4	0.277	8.23 ± 0.02	8.36 ± 0.01	8.31 ± 0.02	6.77 ± 0.03	6.96 ± 0.02	0.96 ± 0.01
5	0.217	8.23 ± 0.01	8.32 ± 0.01	8.28 ± 0.01	6.83 ± 0.02	6.90 ± 0.01	0.93 ± 0.00
6	0.000	8.21 ± 0.00	8.31 ± 0.00	8.27 ± 0.00	6.89 ± 0.00	6.97 ± 0.00	0.95 ± 0.00
7	0.113	8.19 ± 0.00	8.30 ± 0.00	8.25 ± 0.01	6.81 ± 0.01	6.90 ± 0.01	0.96 ± 0.00
8	0.382	8.24 ± 0.01	8.32 ± 0.01	8.28 ± 0.02	6.89 ± 0.03	6.92 ± 0.02	0.93 ± 0.01
9	0.522	8.24 ± 0.01	8.33 ± 0.01	8.29 ± 0.01	6.91 ± 0.03	6.98 ± 0.02	0.94 ± 0.01

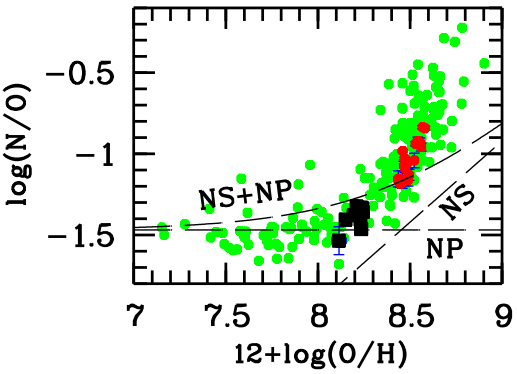

Figure 6. The N/O–O/H diagram for the investigated H II regions in NGC 3963 and NGC 7292. The green circles show T_e-based abundances in the sample of best-studied H II regions in nearby galaxies from the compilation of data of Pilyugin et al. (2010) with additional data from Gusev et al. (2012) and Gusev et al. (2013). The dashed lines show possible boundaries for data points on the N/O–O/H plane under the assumption of a closed-box model for primary (NP), secondary (NS) and both primary and secondary (NS+NP) nitrogen according to Vila-Costas & Edmunds (1993). Chemical abundances of H II regions of our sample based on R-calibration are shown. Other symbols are the same as in Fig. 5.

electron temperature in the nebula essentially depends on the cooling of gas through radiation in the nebular lines, is well known (see the review in Ellison et al. 2008; López-Sánchez & Esteban 2010, for more details). However, it should be noted that O/H, N/H, and t_e are dependent parameters in empirical calibrations. Therefore, we cannot investigate separately any temperature features in studied H II regions.

4 DISCUSSION

4.1 General chemical distribution parameters

In Fig. 8, we compared general parameters of the chemical elements abundances distribution in NGC 3963 and NGC 7292 (central (mean) O/H and N/O, and their gradients) with similar parameters of galaxies of different luminosity and morphology known from the literature.

Zurita et al. (2021b) found that the O/H and N/O gradients–luminosity relations demonstrate different behaviour for strongly barred and unbarred galaxies; strongly barred galaxies show shallow O/H and N/O gradients, whereas these gradients in unbarred and weakly barred galaxies become steeper as the galactic luminosity decreases.

Inspection of Fig. 8 reveals that both NGC 3963 and NGC 7292 follow well the general trends in the diagrams. The giant weakly barred galaxy NGC 3963 lies within the spread of values of Zurita et al. (2021a) on all diagrams, although it has slightly steeper O/H and N/O gradients (see the filled red circles in Fig. 8). Note, if we take formal results of linear fitting for the full sample of H II regions in NGC 3963 (open red circles in Fig. 8), we will find that the galaxy is not distinguished by central O/H and N/O values and their linear gradients from those of sample of Zurita et al. (2021a).

The strongly barred galaxy NGC 7292 belongs to a rare type of galaxies (see Introduction). Data on the abundance of chemical elements have so far been obtained only for a limited number of Magellanic-type galaxies (see e.g. the sample of Pilyugin et al. 2007 in top-left panel of Fig. 8). Among the galaxies studied by Zurita et al. (2021a), only one galaxy, NGC 4395, is close to NGC 7292 in morphology and luminosity. As seen from Fig. 8, NGC 7272 and

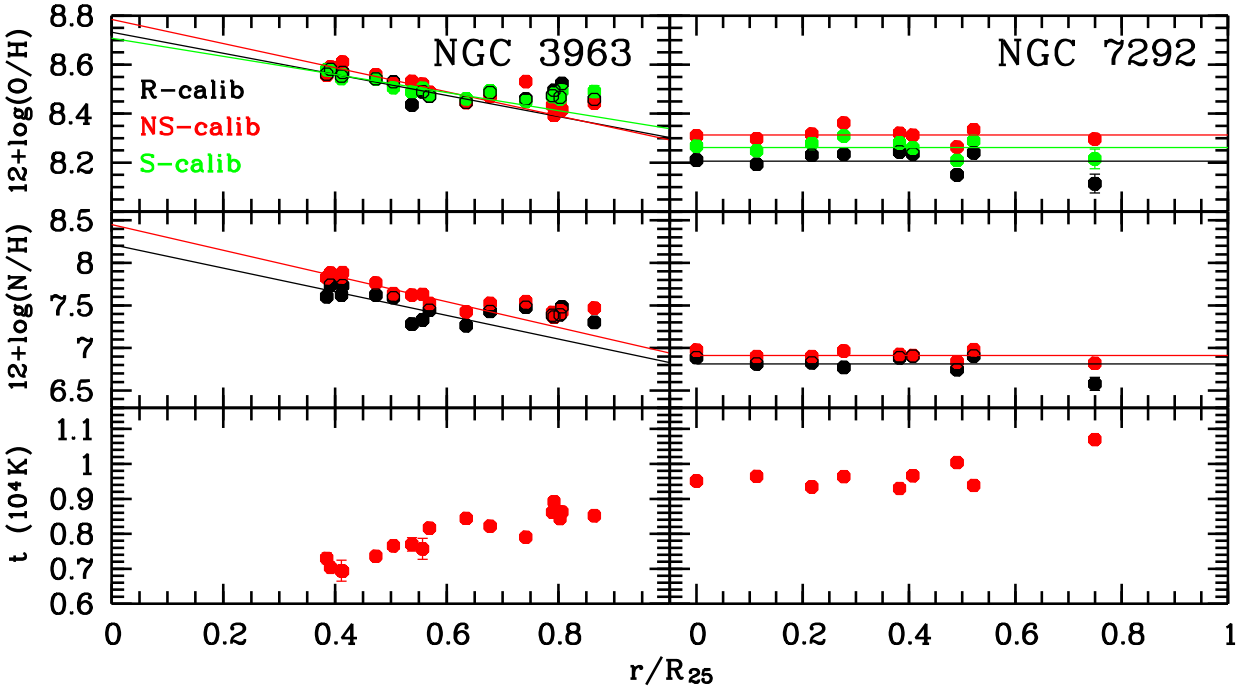

Figure 7. Radial distributions of oxygen abundances (top panels), nitrogen abundances (middle panels), and electron temperatures (bottom panels) in NGC 3963 (left) and NGC 7292 (right) calculated using R- (black), NS- (red), and S-calibrations (green). The solid lines are the best fits to data for NGC 3963 at $r < 0.7R_{25}$ and NGC 7292. The error bars are shown. See the text for details.

Table 6. Parameters of radial distributions of oxygen and nitrogen abundances in the galaxies.

Calibration	$12 + \log(\mathrm{O/H})$			$12 + \log(\mathrm{N/H})$		
	centre	gradient		centre	gradient	
		(dex R_{25}^{-1})	(dex kpc^{-1})		(dex R_{25}^{-1})	(dex kpc^{-1})
			NGC 3963 ($r < 0.7R_{25}$)			
R	8.73 ± 0.09	-0.43 ± 0.09	-0.023 ± 0.005	8.22 ± 0.18	-1.39 ± 0.35	-0.076 ± 0.019
NS	8.78 ± 0.04	-0.49 ± 0.07	-0.027 ± 0.004	8.45 ± 0.09	-1.51 ± 0.18	-0.082 ± 0.010
S	8.71 ± 0.03	-0.37 ± 0.06	-0.020 ± 0.003	–	–	–
			NGC 3963 ($r \geq 0.7R_{25}$)			
R	8.48 ± 0.03	0	0	7.40 ± 0.07	0	0
NS	8.44 ± 0.05	0	0	7.44 ± 0.06	0	0
S	8.47 ± 0.02	0	0	–	–	–
			NGC 7292			
R	8.21 ± 0.05	0	0	6.81 ± 0.11	0	0
NS	8.31 ± 0.03	0	0	6.91 ± 0.06	0	0
S	8.26 ± 0.03	0	–	–	–	–

NGC 4395 have similar central oxygen abundances, central oxygen-to-nitrogen ratios, and O/H and N/O gradients.

4.2 NGC 3963 features

In spite of ordinary general chemical parameters, H II regions in the outer disc of NGC 3963 show the same oxygen and nitrogen abundances within the accuracy of the R-calibration independently of their galactocentic distance (Fig. 7, see also the middle part of Table 6). Moreover, their O/H and N/H abundances, and N/O ratio seem to be slightly higher than those in H II regions from the middle part ($r \approx 0.55R_{25}$) of the NGC 3963 disc. All these H II regions (nos. 17–20, 22, 23) are located in the southern and south-western parts of NGC 3963 (Fig. 1). The deprojected linear distance between the outermost regions (nos. 17 and 23) is 13 kpc. Recall that the object nos. 17–20 were observed using TDS (slit position 3), while the region nos. 22 and 23 were observed using BOSS, i.e. in two independent projects.

As we noted in the Introduction, NGC 3963 has a companion, NGC 3958, which is located at a distance of 110 kpc from NGC 3963 in the SSW direction. This pair has been repeatedly studied in the 21 cm line (van Moorsel 1983; Nordgren et al. 1997). Results of H I data analysis strongly suggest the presence of tidal distortion in both galaxies in the pair (van Moorsel 1983). Actually, features of the H I spatial distribution and the H I velocity field in NGC 3963 can be clearly interpreted as the presence of a powerful gas inflow from the south-western direction (see H I maps and velocity fields for NGC 3963 in van Moorsel 1983; Nordgren et al. 1997). This flow shoves gas behind the nucleus into the north-eastern part of the galaxy.

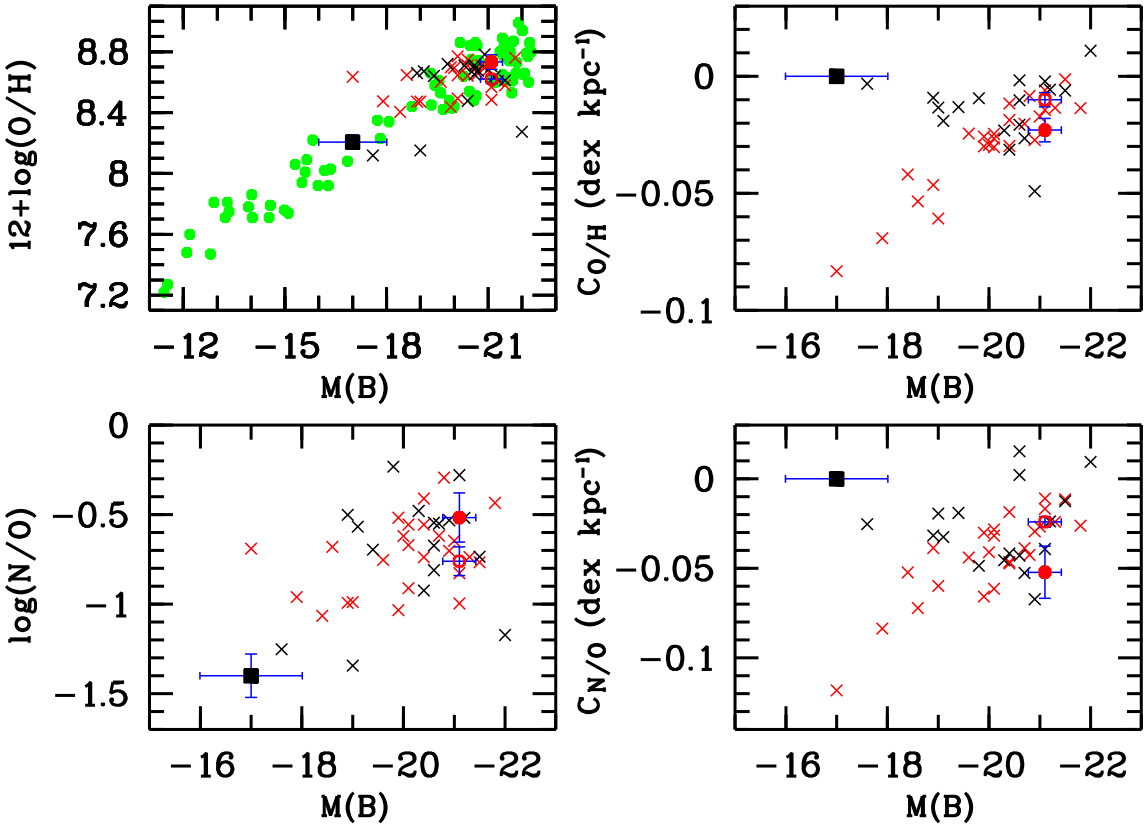

Figure 8. Central (mean) O/H and N/O and their gradients for galaxies of different luminosity. The green circles denote the central oxygen abundances in the discs of spiral galaxies and the oxygen abundances in irregular galaxies from Pilyugin et al. (2007) with additional data from Gusev et al. (2012) and Gusev et al. (2013). The crosses indicate the parameters of strongly barred (black) and unbarred and weakly barred galaxies from Zurita et al. (2021a) obtained using the R-calibration. The filled red circle shows the parameters derived for H II regions sample in the inner disc of NGC 3963 ($r < 0.7R_{25}$), the open red circle denotes the parameters of fitting of full sample of H II regions in NGC 3963, and the black square indicate the mean parameters of chemical abundance distribution in NGC 7292 calculated using the R-calibration. The error crosses are shown. See the text for details.

We assume that the inflow of metal-enriched gas into the south-western part of the galaxy can stimulate star formation in the southern and south-western parts of the outer disc of NGC 3963. As a result, we observe H II regions with the same, comparatively rich chemical abundance. It is possible that this stream is also responsible for the distortion of the southern spiral arm from the form of the classical logarithmic spiral (see Fig. 1).

We do not discuss H II region no. 14 with $r = 0.68R_{25}$, which is located at the end of the northern spiral arm of NGC 3963 (Fig. 1). It has intermediate O/H and N/H abundances between the regions in the inner and the outer discs (Fig. 7), but we have not any other spectral data for H II regions in the outer disc in the northern part of NGC 3963.

4.3 NGC 7292 features

Oxygen and nitrogen abundances usually do not decrease with galactocentric distance in dwarf and irregular galaxies (Richer & McCall 1995; Miller 1996; Hidalgo-Gámez et al. 2001; Pilyugin 2001; Testor 2001; Testor et al. 2003; Peimbert et al. 2005; Hernández-Martínez et al. 2009). NGC 7292 is a good example of an irregular galaxy without radial abundance gradient. However, the chemical elements abundance distribution in NGC 7292 is neither strongly constant nor chaotic.

We noted in Section 3.1 H II region nos. 1 and 4 which are located near the border separating objects with thermal and non-thermal

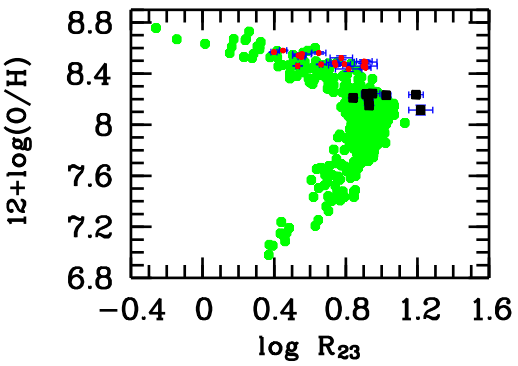

Figure 9. The $\log R_{23}$ − O/H diagram for the sample of H II regions investigated in this study (symbols are the same as in Fig. 5) and taken from the literature (Pilyugin et al. 2012; Gusev et al. 2012, 2013).

emissions on the [N II]λ6584/H α versus [O III]λ5007/H β diagnostic diagram (Fig. 5). Both these regions stand out in the $\log R_{23}$ −O/H diagram (Fig. 9) too.

This diagram, where $R_{23} = I($ [O II]λ3727+3729+ [O III]λ4959 +[O III]λ5007)/I(H β), separates cool rich-oxygen and hot low-oxygen H II regions (see e.g. Pilyugin et al. 2010). If the objects from NGC 3963 occupate the area, where cool rich-oxygen regions, typical for giant galaxies, are located, while most objects from NGC 7292

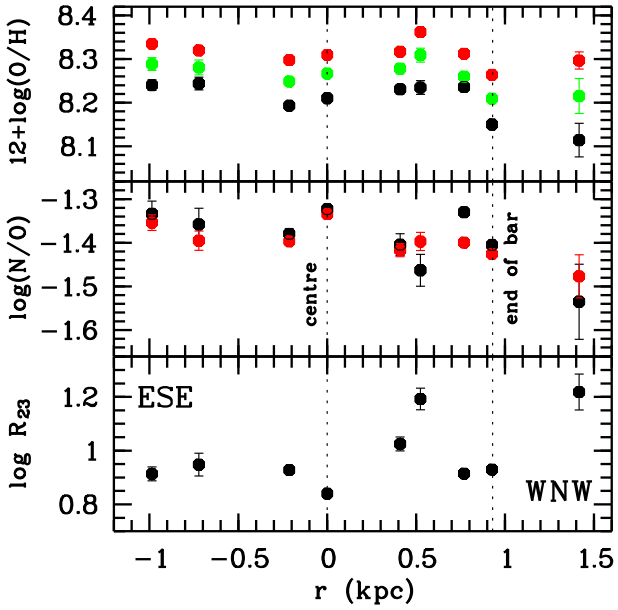

Figure 10. Distributions of oxygen abundance (top), nitrogen-to-oxygen ratio (middle), and $\log R_{23}$ (bottom) along the bar of NGC 7292. Symbols are the same as in Fig. 7. The centre and the end of the bar of the galaxy are indicated by dotted lines. See the text for details.

occupate the area, where warm moderate-metallicity H II regions are located, then region nos. 1 and 4 from NGC 7292 show extremely high R_{23} for any O/H (Fig. 9). This indicates a significant role of the non-thermal (shock) emission in the formation of spectra of these H II regions. Region nos. 1 and 4 are also distinguished by the maximum errors in O/H, N/H, and N/O estimates and the largest differences between O/H, N/H, and N/O values calculated using different calibrations (see Figs 7, 10, Table 5). It is interesting that the region no. 4 is located in the centre of the bar of NGC 7292 at 500 pc from the nucleus and the faint region no. 1 is located in the outer western part of the galaxy (Fig. 1).

We have considered the O/H, N/O, and $\log R_{23}$ distributions along the bar (and the major axis) of NGC 7292 in Fig. 10.

The nucleus (the region no. 6) of NGC 7292 shows the highest N/O ratio among H II regions in the galaxy. The second by brightness region no. 2 (the end of the bar; see Fig. 1) has minimum oxygen abundance and low N/O ratio (Fig. 10). In general, we observe a weak N/O gradient along the major axis of NGC 7292: the N/O ratio decreases from the eastern to the western part of the galaxy (see the middle panel in Fig. 10).

Higher values of N/O correspond to smaller specific star formation rate within an H II region, i.e. star formation in it could have been high in the past, at earlier stage of evolution (Mallery et al. 2007; Mollá & Gavilán 2010). The lower N/O ratios correspond to younger, less evolved H II regions. Thus, the observed N/O gradient may indicate the propagation of a star formation wave along the major axis of NGC 7292 from the east to the west of the galaxy. Unfortunately, the absence of H I and H II velocity fields makes it impossible to develop our hypothesis without additional observational data.

5 CONCLUSIONS

The spectroscopic observations of 32 H II regions in NGC 3963 and NGC 7292, obtained with the 2.5-m telescope of the Caucasus Mountain Observatory of the Sternberg Astronomical Institute with the newly TDS, were carried out.

The oxygen and nitrogen abundances in 26 H II regions are estimated using different empirical calibrations. Parameters of radial distributions of the oxygen and nitrogen abundances in the galaxies are obtained. The chemical elements abundance data for H II regions in NGC 3963 and NGC 7292 are estimated for the first time.

General chemical elements abundances and their distribution in NGC 3963 and NGC 7292 are typical for galaxies with similar luminosities and morphology, wherein both galaxies have some peculiarities in chemical abundance distributions.

H II regions in the outer part of southern spiral arm of NGC 3963 at distances $r > 0.7R_{25}$ show constant, slightly higher oxygen and nitrogen abundances. This can be explained by the inflow of metal-enriched gas into the south-western part of NGC 3963.

Oxygen and nitrogen abundances do not decrease with galactocentric distance in NGC 7292. However, the nitrogen-to-oxygen ratio seems to decrease along the major axis from the eastern to the western part of the galaxy.

ACKNOWLEDGEMENTS

We are grateful to M. A. Burlak (SAI MSU) for help and support during the observations, to O. V. Egorov (Astronomisches Rechen-Institut, Universität Heidelberg and SAI MSU) for helpful comments on different empirical calibrations, and to E. V. Shimanovskaya (SAI MSU) for help with editing this paper. This study was supported by the Russian Foundation for Basic Research (project no 20-02-00080). AVD acknowledges the support by the Interdisciplinary Scientific and Educational School of Moscow University 'Fundamental and Applied Space Research'. The authors acknowledge support from M.V. Lomonosov Moscow State University Program of Development in expanding the instrumentation base of the CMO SAI MSU. The authors acknowledge the use of the HyperLeda data base (http://leda.univ-lyon1.fr), the NASA/IPAC Extragalactic Database (http://ned.ipac.caltech.edu), and The Sloan Digital Sky Survey (http://www.sdss.org).

DATA AVAILABILITY

The SDSS data used in this article are available in the SDSS-DR16 data base at http://skyserver.sdss.org/dr16/. The TDS spectroscopic data can be shared on reasonable request to the corresponding author.

REFERENCES

Baldwin J. A., Phillips M. M., Terlevich R., 1981, PASP, 93, 5
Bresolin F., 2007, ApJ, 656, 186
Bresolin F., Schaerer D., González Delgado R. M., Stasińska G., 2005, A&A, 441, 981
Chiappini V., Romano D., Matteucci F., 2003, MNRAS, 339, 63
Dodin A. V. et al., 2020, Astron. Lett., 46, 429
Dutil D. R., Roy J.-R., 1999, ApJ, 516, 62
Ellison S. L., Patton D. R., Simard L., McConnachie A. W., 2008, AJ, 135, 1877
Ferguson A. M. N., Gallagher J. S., Wyse R. F. G., 1998, AJ, 116, 673
Florido E., Zurita A., Pérez I., Pérez-Montero E., Coelho P. R. T., Gadotti D. A., 2015, A&A, 584, A88
Gusev A. S., Pilyugin L. S., Sakhibov F., Dodonov S. N., Ezhkova O. V., Khramtsova M. S., 2012, MNRAS, 424, 1930
Gusev A. S., Sakhibov F. H., Dodonov S. N., 2013, Astr. Bull., 68, 40
Gusev A. S., Egorov O. V., Sakhibov F., 2014, MNRAS, 437, 1337
Gutiérrez L., Beckman J. E., 2010, ApJ, 710, L44

Hernández-Martínez L., Peña M., Carigi L., García-Rojas J., 2009, A&A, 505, 1027
Hidalgo-Gámez A. M., Olofsson K., Masegosa J., 2001, A&A, 367, 388
Izotov Y. I., Thuan T. X., Lipovetsky V. A., 1994, ApJ, 435, 647
Kauffmann G. et al., 2003, MNRAS, 346, 1055
Kewley L. J., Ellison S. L., 2008, ApJ, 681, 1183
Kewley L. J., Dopita M. A., Sutherland R. S., Heisler C. A., Trevena J., 2001, ApJ, 556, 121
Kobulnicky H. A., Kewley L. J., 2004, ApJ, 617, 240
Kumari N., Maiolino R., Belfiore F., Curti M., 2019, MNRAS, 485, 367
López-Sánchez Á. R., Esteban C., 2010, A&A, 517, A85
Malanchev K. L. et al., 2021, MNRAS, 502, 5147
Mallery R. P. et al., 2007, ApJS, 173, 482
Marcon-Uchida M. M., Matteucci F., Costa R. D. D., 2010, A&A, 520, A35
Marino R. A. et al., 2013, A&A, 559, A114
McCall M. L., Rybski P. M., Shields G. A., 1985, ApJS, 57, 1
Miller B. W., 1996, AJ, 112, 991
Mollá M., Gavilán M., 2010, Mem. Soc. Astron. Ital., 81, 992
Nordgren T. E., Chengalur J. N., Salpeter E. E., Terzian Y., 1997, AJ, 114, 77
Osterbrock D. E., 1989, Astrophysics of Gaseous Nebulae and Active Galactic Nuclei. University Science Books, Mill Valley, CA, p. 422
Pagel B. E. J., 1991, in Oberhummer H., ed., Nuclei in the Cosmos. Springer, Berlin, p. 89
Peimbert A., Peimbert M., Ruiz M. T., 2005, ApJ, 634, 1056
Pérez-Montero E. et al., 2016, A&A, 595, A62,
Pettini M., Pagel B., 2004, MNRAS, 348, L59
Pilyugin L. S., 2001, A&A, 374, 412
Pilyugin L. S., Grebel E. K., 2016, MNRAS, 457, 3678
Pilyugin L. S., Mattsson L., 2011, MNRAS, 412, 1145
Pilyugin L. S., Thuan T. X., 2005, ApJ, 631, 231
Pilyugin L. S., Thuan T. X., Vílchez J. M., 2007, MNRAS, 376, 353
Pilyugin L. S., Vílchez J. M., Thuan T. X., 2010, ApJ, 720, 1738
Pilyugin L. S., Grebel E. K., Mattsson L., 2012, MNRAS, 424, 2316
Pilyugin L. S., Grebel E. K., Kniazev A. Y., 2014, AJ, 147, A131
Poetrodjojo H., D'Agostino J. J., Groves B., Kewley L., Ho I.-T., Rich J., Madore B. F., Seibert M., 2019, MNRAS, 487, 79
Potanin S. A. et al., 2020, Astron. Lett., 46, 836
Proxauf B., Öttl S., Kimeswenger S., 2014, A&A, 561, A10
Richer M. G., McCall M. L., 1995, ApJ, 445, 642
Sánchez S. F. et al., 2014, A&A, 563, A49
Sanders R. L., Shapley A. E., Zhang K., Yan R., 2017, ApJ, 850, 136
Searle L., 1971, ApJ, 168, 327
Storey P. J., Zeippen C. J., 2000, MNRAS, 312, 813
Testor G., 2001, A&A, 372, 667
Testor G., Lemaire J. L., Field D., 2003, A&A, 407, 905
Tully R. B., Rizzi L., Shaya E. J., Courtois H. M., Makarov D. I., Jacobs B. A., 2009, AJ, 138, 323
van Moorsel G. A., 1983, A&AS, 53, 271
Vila-Costas M. B., Edmunds M. G., 1992, MNRAS, 259, 121
Vila-Costas M. B., Edmunds M. G., 1993, MNRAS, 265, 212
Zaritsky D., Kennicutt R. C., Huchra J. P., 1994, ApJ, 420, 87
Zinchenko I. A., Just A., Pilyugin L. S., Lara-Lopez M. A., 2019, A&A, 623, A7
Zurita A., Florido E., Bresolin F., Pérez-Montero E., Pérez I., 2021a, MNRAS, 500, 2359
Zurita A., Florido E., Bresolin F., Pérez I., Pérez-Montero E., 2021b, MNRAS, 500, 2380

This paper has been typeset from a TEX/LATEX file prepared by the author.